Journal of Hydrology: Regional Studies 42 (2022) 101134

Contents lists available at ScienceDirect

Journal of Hydrology: Regional Studies

journal homepage: www.elsevier.com/locate/ejrh

Hydrological evaluation of radar and satellite gauge-merged precipitation datasets using the SWAT model: Case of the Terauchi catchment in Japan

Slim Mtibaa [*,1], Shiho Asano

Department of Disaster Prevention, Meteorology and Hydrology, Forestry and Forest Products Research Institute, Tsukuba, Japan

ARTICLE INFO

Keywords:
Streamflow simulation
Weather radars
GsMAP
Gauge-merged
SWAT model

ABSTRACT

Study region: The Terauchi catchment, southwestern Japan
Study focus: This paper evaluates two gauge-merged precipitation datasets derived from weather radars (R/A) and satellites (GsMAP_G) based on their capability to improve streamflow simulation using the Soil and Water Assessment Tool (SWAT) model. A third dataset includes measurements from local rain gauges used for producing the R/A database but not the GsMAP_G product was prepared for comparison reasons. The R/A and GsMAP_G data were first compared to gauge observations. The performance and prediction uncertainty of the SWAT model forced by the evaluated datasets were subsequently quantified and compared.
New hydrological insights for the region: The R/A dataset overestimated the precipitation, while the GsMAP_G underestimated it. After calibration, the R/A performed best (NSE = 88–91%), followed by the Gauge (NSE = 84%) and GsMAP_G (NSE = 54%) scenarios. The R/A product improved the overall simulation performance by 6.50% and 62.40% in terms of NSE and absolute percent bias compared to the Gauge model. The performance of the evaluated datasets varied depending on streamflow occurrence exceedance probability (OEP). The R/A dataset improved the simulation of extremely high (OEP < 1%) and low (OEP > 60%) streamflow events as it resulted in the lowest simulation biases and errors. The current investigation suggests the use of the R/A product for improving the simulation of daily streamflow, including hydro-climatic extremes.

1. Introduction

Hydrological models simulate water balance components to understand the various hydrological processes (Ogden, 2021). These tools support managing water resources, forecasting extreme hydrological events (i.e., floods and debris flow), and developing mitigation measures (Devia et al., 2015; Li et al., 2018; Singh, 2018; Tan et al., 2020). Therefore, reliable outputs are always sought by stakeholders. This need requires a correct representation of models' inputs at the spatial and temporal scales. Among these parameters, precipitation is the key driving force in simulating streamflow dynamics (Tuo et al., 2016) and the primary source of prediction uncertainty in many hydrological models (Chao et al., 2018; Yang et al., 2017). Thus, accurate data and adequate representation of precipitation variability are crucial for precise simulation outputs and effective decision-making.

* Corresponding author.
E-mail address: mtibaaslim@ffpri.affrc.go.jp (S. Mtibaa).
[1] 1 Matsunosato, Tsukuba, Ibaraki 305-8687, Japan.

https://doi.org/10.1016/j.ejrh.2022.101134
Received 27 December 2021; Received in revised form 19 May 2022; Accepted 5 June 2022
Available online 14 June 2022

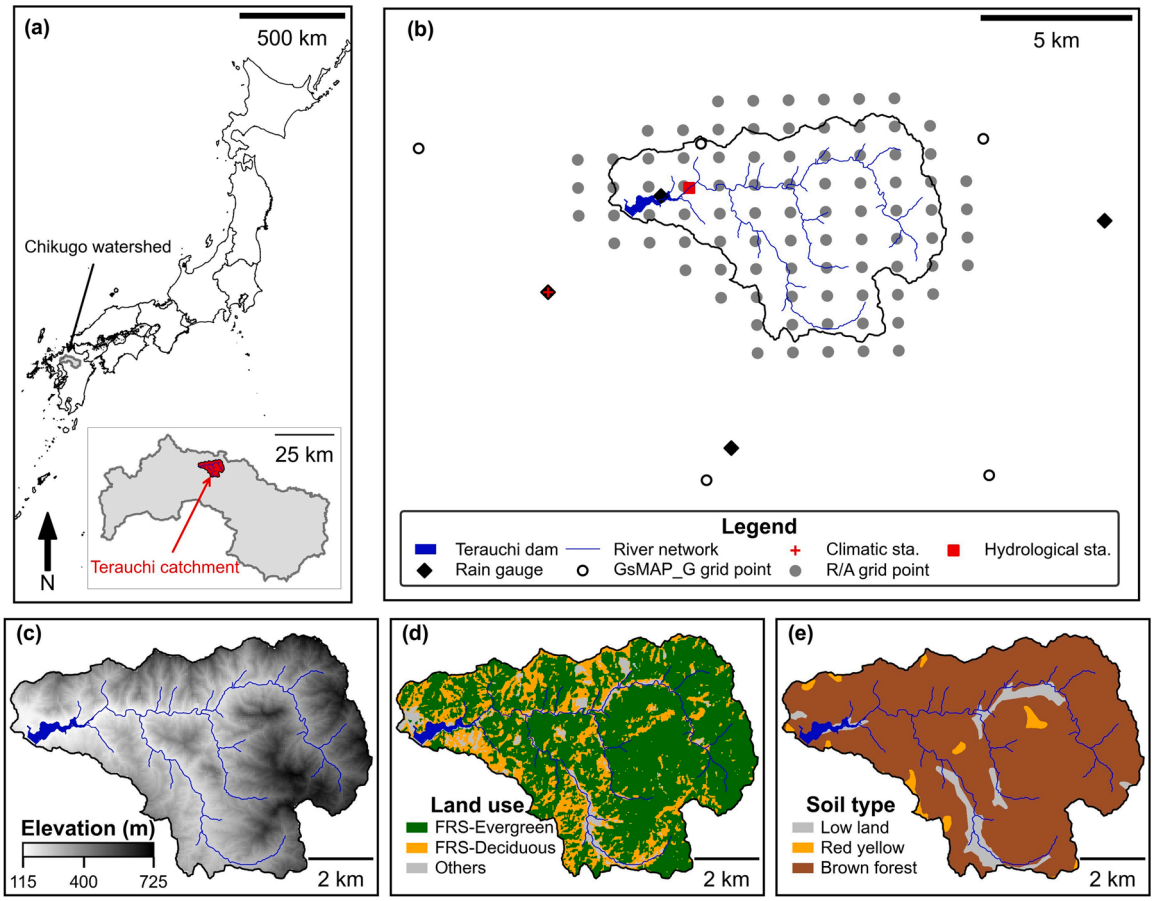

Fig. 1. Geographic location of the Terauchi catchment (a) and SWAT input data (b–e).

Balancing between the accuracy and spatial representation of precipitation data in hydrological models is still challenging (Dembélé et al., 2020). Indeed, the precipitation is traditionally measured using rain gauges (Sun et al., 2018), which provide accurate observations at a point-scale of 20 cm diameter. These measurements are often treated as the "truth" rainfall value (Tapiador et al., 2017). However, they may become uncertain when the point-scale observations are extended to ungauged areas due to a sparse rain gauge network (Deng et al., 2019; Yang et al., 2017). The uncertainty increases in environments with complex terrains (e.g., mountainous catchments) and extreme climates (e.g., convective rainfalls, tropical cyclone rainfalls) (Li et al., 2019; Schroeer et al., 2018; Strauch et al., 2013). Rainfall in such regions presents high spatial and temporal variability, making the assumption of spatially uniform rainfall in hydrological models invalid (Cho et al., 2009). In addition, rain gauge measurements may exhibit significant negative bias during windy weather and intense rainfall conditions that generate water losses and erratic behavior of the gauge system (Cha and Lee, 2021; Tobin and Bennett, 2009; Zhong et al., 2016). These drawbacks lead to an inaccurate spatial representation of the precipitation that may impact the simulation outputs.

Advances in remote-sensing technologies (weather radars and satellites) make up for the limitations of rain gauges by allowing a spatial observation of the precipitation. These technologies provide rainfall estimates with high spatial and temporal resolutions at global and regional scales (Sun et al., 2018) that can emerge as promising alternatives for gauge-based data in hydrological models. Several studies have evaluated the performance of radar and satellite precipitation products using the Soil and Water Assessment Tool (SWAT) model (Arnold et al., 1998), as it is one of the most acknowledged models (Tan et al., 2021 and references therein). The studies' findings showed the usefulness of these alternatives in simulating hydrological processes. However, it has been stressed that satellites and radars only based datasets resulted in unsatisfactory daily streamflow simulation performances due to substantial rainfall estimation errors.

Merging the advantages of rain gauges in radar and satellite products is an effective strategy for overcoming precipitation uncertainty while preserving spatial coverage (Ochoa-Rodriguez et al., 2019). Different methods and algorithms applied to radar and satellite products have remarkably improved the quality of precipitation estimates and reduced the substantial rainfall underestimation (Chao et al., 2018; Goudenhoofdt and Delobbe, 2009; Li et al., 2015; McKee and Binns, 2016; Yang et al., 2017). The Gauge-calibrated Global Satellite Mapping of Precipitation (GsMAP_G) developed by the Japan Aerospace Exploration Agency (JAXA) and the Radar/rain gauge Analyzed precipitation (R/A) produced by the Japanese Meteorological Agency (JMA) are two

gauge-merged products commonly used for hydrometeorological forecasting in Japan. Most previous evaluations focused on the potential of these datasets to detect and estimate precipitation (e.g., Hirokawa et al., 2020; Ishizaki and Matsuyama, 2018; Mega et al., 2019; Suzuki et al., 2017; Tashima et al., 2020). The potential of the GsMAP_G in simulating streamflow using the SWAT model was evaluated only in a few works and limited over catchments in China and Southeast Asia (Deng et al., 2019; Dinh et al., 2020; Zhang et al., 2020), while the potential of the R/A product has not yet assessed.

In this study, we evaluated the potential of the GsMAP_G and R/A precipitation datasets to simulate daily streamflow using the SWAT model in the Terauchi watershed, a forested headwater catchment in southwestern Japan. The SWAT model was also applied using a gauge precipitation dataset that served for comparison. The first part of the investigation compares the GsMAP_G and R/A datasets with gauge observations at grid and catchment scales. The second part assesses the performances of the SWAT model forced by the three precipitation datasets in terms of prediction accuracy and uncertainty. The results of the present investigation should provide insights into the potential of the GsMAP_G and R/A products in simulating daily streamflow using the SWAT model in a mountainous catchment with an extreme climate.

2. Study site and precipitation datasets

2.1. The Terauchi catchment

This study focused on the Terauchi watershed in southwestern Japan (Fig. 1a). The catchment was selected because it is a headwater of the Chikugo river basin, and therefore its streamflow is not significantly influenced by hydropower production or anthropogenic activities. Furthermore, the area experienced frequent convective rainstorms during the rainy season in summer (May–July) and the Typhoon season in autumn (August–October). The catchment drains approximately 51 km^2 to the Terauchi dam, constructed downstream for flood protection and water supply purposes. The study area is dominated by dense evergreen forests (around 88%) (FRS-Evergreen in Fig. 1d) and brown forest soils (approximately 92%) (Fig. 1e), with an elevation varying between 115 and 725 m a.s.l (Fig. 1c). The climate is humid and subtropical with rainy summers. Mean annual precipitation and average temperature recorded from 2010 to 2019 at the Asakura station, located approximately 10 km to the southwest of the catchment, were 2058 mm and about 16 °C, respectively.

2.2. Precipitation datasets

2.2.1. Gauge precipitation dataset

In Japan, the rain gauge network comprises thousands of rain gauges operated by the Japanese Meteorological Agency (JMA) and the Ministry of Land, Infrastructure, Transport, and Tourism (MLIT) of Japan. There are approximately 1300 weather stations, with an average interval of 17 km, operated by the JMA (Kawase et al., 2019). This network is known as the Automated Meteorological Data Acquisition System (AMeDAS). The MLIT network comprises about 2800 rain gauges used for flood control and river management. Only four rain gauges are located in and around the Terauchi catchment and, accordingly, were selected in the current study (Fig. 1b). Rainfall data recorded before 2010 by one of the selected rain gauges are incomplete. Therefore, we focused on the period 2010–2019 as an assessment period to ensure the completeness of all rainfall data.

2.2.2. Radar/rain gauge analyzed precipitation dataset

The Japanese weather radar network includes 46 C-band radars operated by the JMA and MLIT. Weather radars emit microwaves, within a radius of hundreds of kilometers, via a rotating antenna and observe the reflected echo intensities and Doppler velocities every five minutes. The backscattered signals are processed, converted into precipitation estimates, and merged with ground rain gauges to produce the Radar/Rain gauge-Analyzed precipitation (R/A) dataset (Nagata, 2011). This product provides hourly cumulative rainfall with a spatial resolution of 5 km (1988–2001), 2.5 km (2001–2005), and 1 km (from 2006). The 5-km and 2.5-km R/A datasets were produced based on data from 20 weather radars and the AMeDAS rain gauges. Since 2006, the spatial resolution and prediction accuracy of the R/A dataset has been improved due to including data from 26 weather radars managed by MLIT and more rain gauges operated by MLIT and local governments in the processing algorithm (Ishizaki and Matsuyama, 2018). Suzuki et al. (2017) assessed the accuracy of the 1-km R/A dataset by comparing daily precipitation estimates with rainfall measurements at 498 rain gauges not included in the R/A calibration algorithm from 2006 to 2013 and found a good correlation coefficient ($r > 0.87$). Therefore, it may accurately represent the spatial precipitation variability within the study area. For evaluating the potential of the 1-km R/A dataset in streamflow simulation, we extracted the time series data (2010–2019) for each grid located inside and around the Terauchi catchment (Fig. 1b). Then, we used it as rainfall inputs in the SWAT model.

2.2.3. Gauge-adjusted Global Satellite Mapping of Precipitation dataset

The Global Satellite Mapping of Precipitation (GsMAP) project combines multiple satellite-based precipitation estimates from passive microwave sensors and infrared radiometers to develop global hourly rainfall maps with a resolution of 0.1° (Kubota et al., 2009). It is operated by the Japan Aerospace Exploration Agency (JAXA) under the Global Precipitation Measures (GPM) mission. The GsMAP project provides different precipitation products (standard, near-real-time, real-time, and reanalyzed) with and without gauge adjustment. These databases are produced by algorithms retrieving global precipitation estimates from satellites. We employed the standard gauge-calibrated GsMAP product (GsMAP_G) produced by the GsMAP algorithm Ver. 6.0 as input for the SWAT model by extracting the times series for each grid cell located inside and around the study area for 2010–2019 (Fig. 1b). This retrieval algorithm

Table 1
Input data for the SWAT model.

Input data	Format	Resolution (spatial/ temporal)	Description and sources
Topographic	Raster	10 m / NA	A digital elevation model (DEM) developed by the Geospatial Information Authority of Japan (GSI) from 1/25 000 topographic maps.
Land use	Raster	30 m / NA	The high-resolution land use and land cover map products (version 16.09), developed by the Japan Aerospace Exploration Agency (JAXA) from multiple remote sensed data. Available on https://www.eorc.jaxa.jp/ALOS/en/lulc/lulc_jpn.htm.
Soil	Raster	10 m / NA	The new soil map of Japan (1/200 000 scale) developed by the National Institute for Agro-Environmental Sciences in Japan (Obara et al., 2016)
Climate	Text	1 station/ daily	The temperature and wind speed data are provided by the Asakura station (operated by the JMA)

uses various attributes derived from the Tropical Rainfall Measuring Mission (TRMM) Precipitation Radar (PR) to improve precipitation detection. Furthermore, it adjusts the 24 h accumulated precipitation estimates to daily rain rates provided by the NOAA Climate Prediction Center (CPC) Gauge-based Analysis of Global daily precipitation data (Tashima et al., 2020) to improve precipitation estimation. This latter includes more than 16 000 rain gauges (Chen et al., 2008), and none of them is located in or around our study area. Further information on the algorithm used for calibrating precipitation estimates is available in the algorithm theoretical basis document developed by the algorithm development team in JAXA (JAXA, 2014).

3. Methods

3.1. SWAT model

3.1.1. General description

The SWAT model, developed by the Agricultural Research Service of the United States Department of Agriculture (USDA), is a semi-distributed process-based model (Arnold et al., 1998). It is operated on a watershed scale to simulate the time-continuous changes in hydrological processes, erosion, vegetation yield, and water quality and evaluate the impacts of land management practices.

The model requires geospatial (topographic, land-use, and soil data) and temporal data (precipitation, temperature, wind speed, humidity, and solar radiation). First, the model uses the topographic data for delineating the study watershed after defining the watershed outlet. Then, it discretizes the watershed into multiple sub-basins depending on the Threshold Drainage Area (TDA). TDA reflects the minimum upstream drainage area for channel origination (Lin et al., 2020). Subsequently, each sub-basin is subdivided into multiple lumped land units comprising unique land cover type, soil class, and slope combinations, known as Hydrological Response Units (HRUs).

All the processes in the SWAT model (e.g., hydrology, sediment dynamics, plant growth, and nutrients…) are governed by the water balance equation (Arnold et al., 2012) (Eq. 1):

$$SW_t = SW_0 + \sum_{i=1}^{t} \left(R_{day} - Q_{surf} - E_a - W_{seep} - Q_{gw}\right) \quad (1)$$

where SW_t is the final soil water content (mm), SW_0 is the initial soil water content on day i (mm), t is the time (days), R_{day} is the amount of precipitation on day i (mm), Q_{surf} is the amount of surface runoff on day i (mm), E_a is the amount of evapotranspiration on day i (mm), W_{seep} is the amount of water entering the vadose zone from the soil profile on day i (mm), and Q_{gw} is the amount of return flow on day i (mm). Detailed information on the simulation methods is available in the theoretical documentation of the SWAT model (Neitsch et al., 2011).

3.1.2. Model setup and inputs

This study uses the ArcSWAT 2012 interface (version 2012.10_4.24) to set up and parameterize the SWAT model. The model inputs are listed and described in Table 1. Soil information was obtained from the soil database of the National Institute for Agro-Environmental Sciences, Japan (Obara et al., 2016). Additionally, the soil bulk density was estimated using Nanko et al. (2014) method. Based on the DEM analysis, a TDA of 100 ha was used for discretizing the study area into 18 sub-basins. Subsequently, the thresholds of HRU definition were set to 10% for land use, soil, and slope classes, resulting in 72 HRUs.

Three precipitation datasets (Gauge, R/A, GsMAP_G), as described in Section 2.2, have been used in this work. We applied the SWAT model on a daily time step from 2010 to 2019. The first two years served as an equilibrium period to stabilize the initial soil water conditions (Abbaspour et al., 2015). In each simulation, the surface runoff was estimated using the curve number method developed by the Soil Conservation Service (SCS, 1972). The evapotranspiration was calculated using the Hargreaves method requiring only temperature data (Hargreaves et al., 1985).

3.1.3. Model calibration and validation

The model was calibrated from 2012 to 2015 and validated from 2016 to 2019 for daily streamflow, using observed daily discharge data at the outlet of the Terauchi catchment. These two durations were selected based on the average daily streamflow observed during

Table 2
Hydrological parameters used in the auto-calibration process and their controls on streamflow simulation (*"v" means a replacement, and "r" stands for a relative change to the initial parameters values*).

Parameter	Controls	Default value	Initial calibration ranges
r_CN2	Surface runoff volume in the total streamflow	55 – 92	±50%
r_SOL_AWC	Soil water content	0.078 – 0.1	±50%
r_SOL_BD	Soil water content	0.9 – 1.14	±50%
r_SOL_K	Amount of water that percolates out of the soil profile	784 – 1166	±50%
r_SLSUBBSN	Overland flow time of concentration	9.1 – 91	±50%
r_HRU_SLP	Overland flow time of concentration	0.03 – 0.8	±50%
v_OV_N	Overland flow time of concentration	0.01 – 0.1	0.01–30
v_EPCO	Water uptake by plants	1	0 – 1
v_ESCO	Soil water evaporation rate	0.95	0 – 1
v_LAT_TTIME	Lateral flow contribution to the total streamflow	0	0 – 180
v_CH_N2	Channel flow time of concentration	0.014	0.025 – 0.15
v_CH_K2	Volume of streamflow lost via transmission losses from the main channel	0	6 – 76
v_ALPHA_BNK	Bank storage contribution to the total streamflow via return flow	0	0 – 1
v_GWQMN	Groundwater flow contribution to the total streamflow	1000	0 – 5000
v_GW_DELAY	Volume of water recharged to shallow and deep aquifers	31	1 – 500
v_REVAPMN	Volume of water removed from the shallow aquifer by evapotranspiration	750	0 – 1000

both periods, which did not change significantly. Before the calibration phase, we performed a sensitivity analysis for several parameters that control the hydrological processes in the SWAT model. The objective was to avoid over-parameterization and determine the sensitive parameters in the Terauchi catchment (Arnold et al., 2012). The analysis was done using the Latin hypercube one-at-a-time (LH-OAT) method included within the Sequential Uncertainty Fitting (SUFI2) procedure of the SWAT Calibration Uncertainty Program (SWAT-CUP). The LH-OAT assesses the model sensitivity to a given parameter by varying the values of this parameter within a predefined uncertainty range while keeping the other parameters constant. A detailed description of the method is available in Abbaspour (2014).

The baseflow recession factor (ALPHA_BF) that partitions the total streamflow into surface runoff and baseflow was the most sensitive parameter in the Terauchi catchment. To reliably adjust this parameter and avoid the impact of auto-calibration on streamflow simulation, the ALPHA_BF was fixed to 0.0415 in the three evaluated scenarios. This value was retrieved using the automated flow separation method developed by Arnold et al. (1995) and the 10-year streamflow observations. It indicates slow drainage and large storage in shallow aquifers (Wu and Johnston, 2007). The auto-calibration step involved the other sensitive parameters that impact streamflow modeling by controlling the different hydrological processes (Table 2). It was performed, with four iterations of 1000 simulations each, using the SUFI2 method. In the first iteration, the initial parameters' intervals were quantified to physically-reasonable uncertainty based on SWAT documentation (Neitsch et al., 2011). After each iteration, these intervals were narrowed to the new uncertainty ranges suggested by the SUIFI2 procedure.

The validation step evaluates the capability of the calibrated model to make sufficiently accurate streamflow simulations (Arnold et al., 2012). It was performed using the fitted parameters obtained after the fourth calibration iteration and observed streamflow for 2016–2019.

3.2. Comparison of the precipitation datasets

We evaluated the R/A and GsMAP_G precipitation datasets at grid and catchment scales for 2010–2019. The daily data at four grid points, where the rain gauges are located, were extracted and compared with the gauge measurements using three quantitative statistics: (1) the Pearson correlation coefficient (r) measures the degree of collinearity; (2) the percent bias (PBIAS) computes the average tendency of the merged datasets. Here, negative values mean that the GsMAP_G or R/A data are higher than the gauge measures; (3) the Root Mean Square Error (RMSE) computes the differences. The equations used for calculating these metrics are available in Appendix A. Furthermore, we computed three categorical statistic metrics to assess the rainfall detection capabilities of the R/A and GsMAP_G products. These indicators are the probability of detection (POD), false alarm ratio (FAR), and critical success index (CSI). The POD reveals the fraction of correctly detected precipitation occurrences. The FAR indicates the fraction of falsely detected rains. The CSI represents the overall rains correctly detected by the GsMAP or R/A products. The calculation methods are based on a 2×2 contingency table (Wilks, 2011) and are detailed in Appendix A.

At the catchment scale, we first examined the daily precipitation inputs in the different models based on the empirical cumulative distribution function (CDF). Then, we evaluated the monthly variation of PBIAS and RMSE that compared daily precipitation inputs from the R/A and GsMAP_G products with those derived from the Gauge dataset.

3.3. Hydrological evaluation of the precipitation datasets

We evaluated the usefulness of the two gauge-merged precipitation datasets in streamflow simulation by comparing the outputs of the R/A and GsMAP_G scenarios to the Gauge scenario and streamflow observations. The comparison examines the model performance and prediction uncertainty.

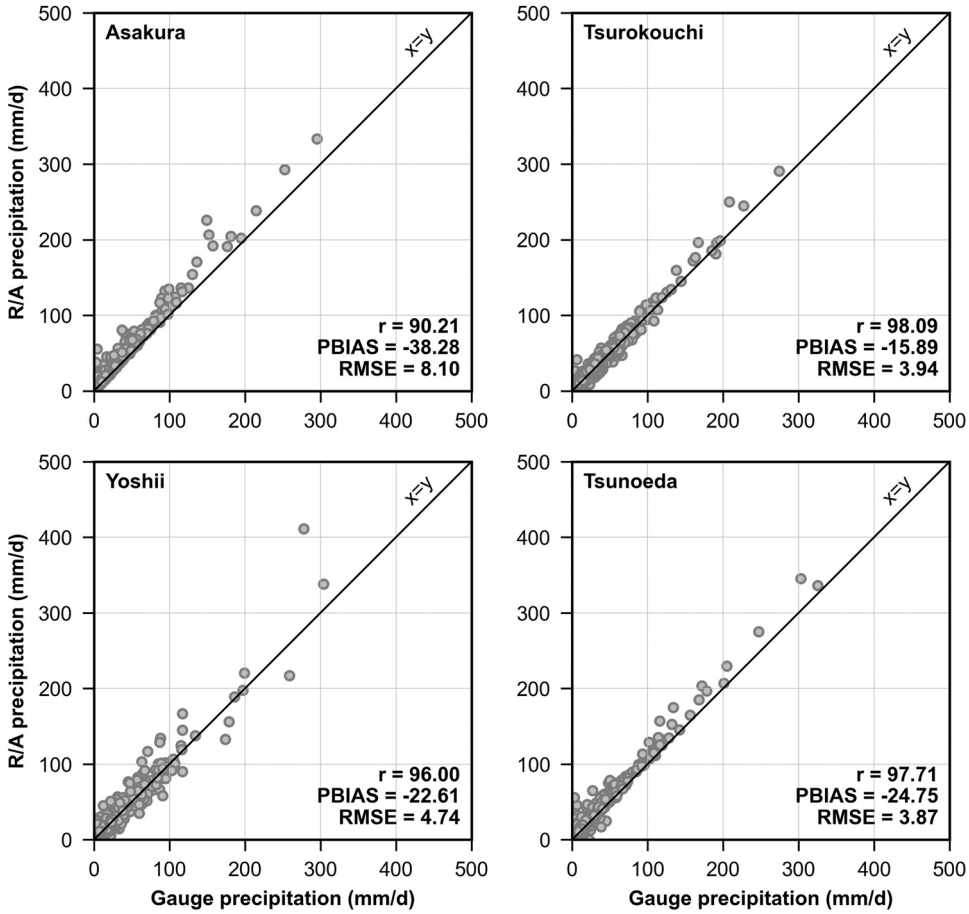

Fig. 2. Scatterplots of daily precipitation data from the Gauge and R/A datasets.

3.3.1. *Model performance*

The model performance was assessed by evaluating the goodness of fit between simulated and observed streamflow using four statistical indicators: (1) the Nash and Sutcliffe Efficiency (NSE) coefficient that calculates the quantity differences between the simulated streamflow and the observations (Nash and Sutclifee, 1970). (2) the PBIAS that indicates an overestimation in the case of a negative value; (3) the RMSE-observations standard deviation ratio (RSR) static that standardizes the RMSE between simulated and observed streamflow to the standard deviation of the observations; (4) the coefficient of determination (R^2) that describes the degree of collinearity between simulated and observed streamflow. Calculation equations are available in Appendix A. According to the values of these four statistical indicators, the model performance was further judged following the performance evaluation criteria recommended by Moriasi et al., (2007, 2015). For instance, the model performance is deemed as "satisfactory" for flow simulation if $0.60 < R^2 \leq 0.75$, $0.50 < NSE \leq 0.70$, $\pm 10 < PBIAS \leq \pm 15$, and $0.60 < RSR \leq 0.70$.

3.3.2. *Model prediction uncertainty*

Uncertainties in streamflow simulation can be due to uncertain model inputs and parameters (Abbaspour et al., 2015). Biases in precipitation accuracy and spatial representation account for most of this uncertainty (Chao et al., 2018; Gassman et al., 2007). Therefore, it is crucial to evaluate the prediction uncertainty associated with the different precipitation inputs.

In each scenario, the streamflow prediction uncertainty was expressed as the final intervals of the calibrated parameters used by the SUIFI2 procedure at the final iteration of model calibration. The SUIFI2 algorithm considers the 95% prediction uncertainty (95PPU) at 2.5% and 97.5% of the cumulative probability distribution of the simulated streamflow derived through the Latin Hypercube sampling. Accordingly, the model performance is represented by a set of good solutions expressed by the 95PPU instead of a single solution (best simulation) (Abbaspour et al., 2015). The prediction uncertainty is assessed by computing two statistical indices: P-factor and R-factor (Abbaspour et al., 2004). P-factor represents the fraction of observed streamflow enveloped by the 95PPU. A P-factor = 1 indicates that all the observations are bracketed by the 95PPU band. R-factor measures the thickness of the 95PPU band. It computes the ratio of the average width of the 95PPU and the standard deviation of the observed streamflow. A prediction uncertainty is acceptable if P-factor > 0.70 and R-factor < 1.5 (Abbaspour et al., 2015).

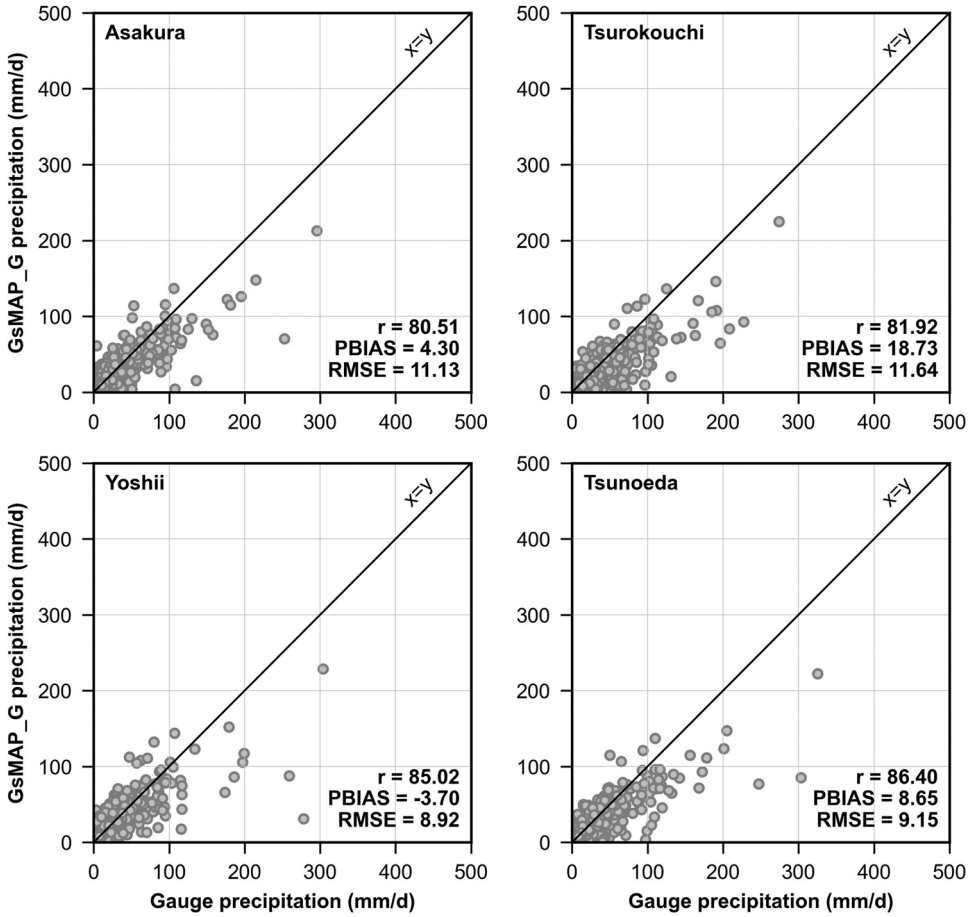

Fig. 3. Scatterplots of daily precipitation data from the Gauge and GsMAP_G datasets.

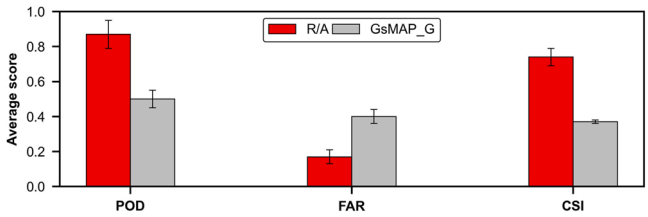

Fig. 4. Categorical statistic metrics for daily precipitation data from the R/A and GsMAP_G products.

4. Results

4.1. Comparison of precipitation datasets

The scatter plots in Figs. 2 and 3 compare daily precipitation data from the R/A and GsMAP_G datasets with rain gauge observations for 2010–2019. The precipitation data estimated by the two gauge-merged datasets were in good agreement with those measured by rain gauges ($r > 90\%$ for the R/A dataset and $r > 80\%$ for the GsMAP_G dataset). The R/A dataset overestimated daily rainfall (PBIAS $= -38.28$ to -15.89%). Conversely, the GsMAP_G dataset underestimated the precipitation (PBIAS $= 4.30$–18.73%), except at the Yoshii station. This underestimation was well noted for precipitation > 100 mm/d and convective rainfall events experienced in the area (e.g., rainfall events of 2017/07/05, 2012/07/14, and 2010/07/13). Compared to the R/A dataset, the GsMAP_G dataset exhibited larger errors in estimating the precipitation (RMSE $= 8.92$–11.64 mm/d).

The categorical indicators computed using a rain/no-rain threshold of 1 mm at the four rain gauges are illustrated in Fig. 4. The R/A dataset outperformed the GsMAP_G product in detecting rainfall during the observation period. The R/A dataset exhibited good rainfall detection scores (average POD $= 0.87$, average FAR $= 0.17$, average CSI $= 0.75$), demonstrating its ability to correctly detect

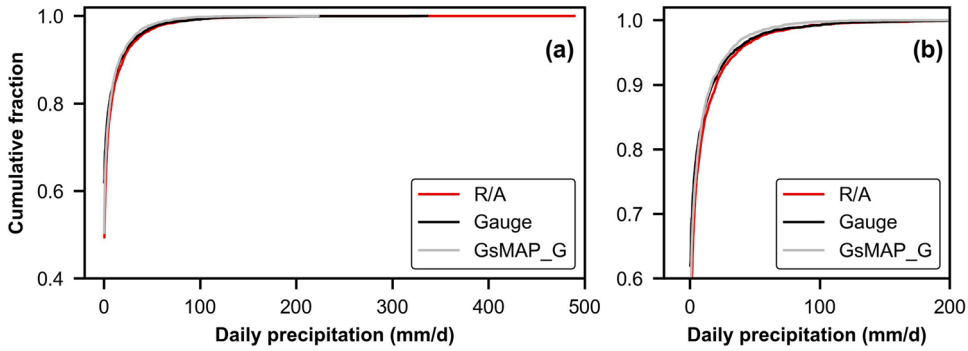

Fig. 5. Empirical cumulative distributions of daily precipitation of the Gauge, R/A, and GsMAP_G inputs in the Terauchi catchment.

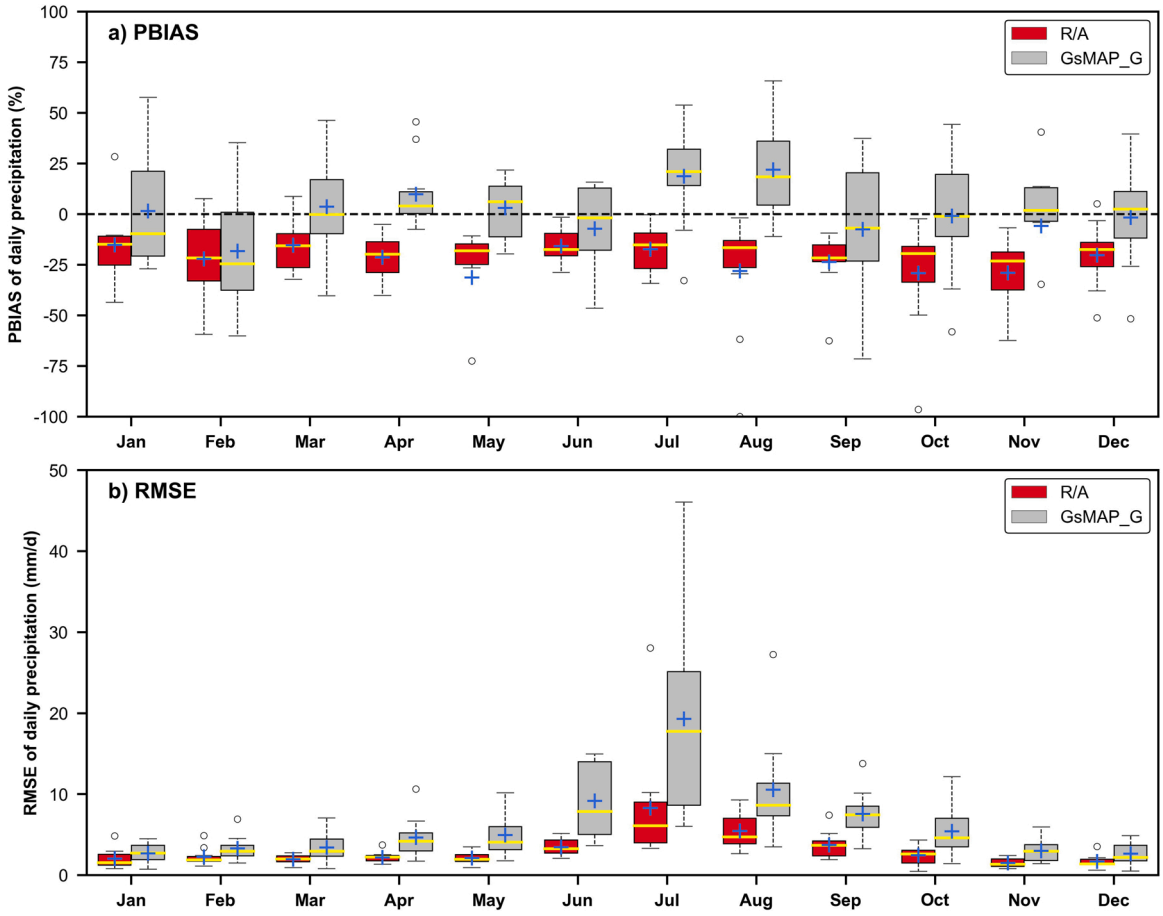

Fig. 6. Box and whisker plot of differences between daily precipitation averaged over the Terauchi catchment from the two merged precipitation products and the Gauge dataset in terms of PBIAS (a) and RMSE (b) (yellow line shows the median, blue plus mark '+' displays the mean).

rainy days. On the other hand, the GsMAP product presented lower rainfall detection accuracy with an average POD of 0.50 and an average FAR of 0.40, resulting in a low average CSI of 0.37.

At the catchment scale, the daily precipitation inputs averaged over the Terauchi catchment from the three datasets are compared in Fig. 5. The three precipitation datasets exhibited different occurrence probabilities for dry and rainy days. The highest difference was for the occurrence of dry days (precipitation = 0). The R/A and GsMAP_G datasets indicated a lower chance of dry days (about 40%) than the gauge dataset (about 60%). The occurrence probabilities of rainy days with less than 200 mm of precipitation did not differ significantly (Fig. 5b). The fractions of rainy days with extreme daily precipitation (rainfall > 200 mm/day) were low. Compared to the rain gauge scenario, the R/A dataset overestimated the intensities of these extremes, while the GsMAP_G product

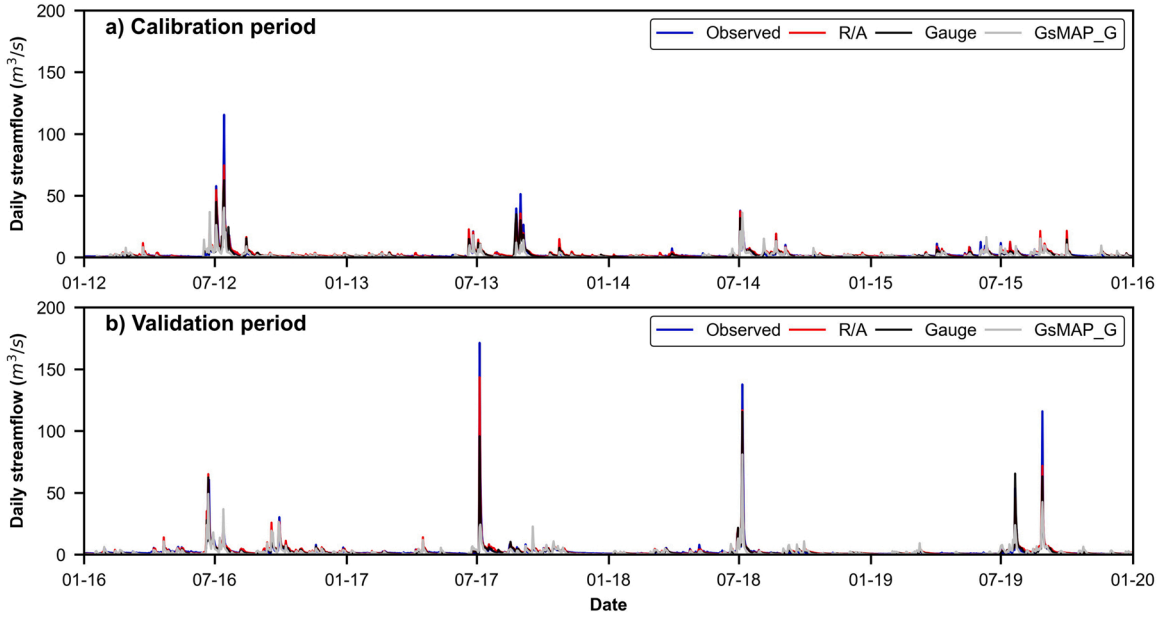

Fig. 7. Simulated and observed daily streamflow during calibration (a) and validation (b) periods.

Table 3
Performance of the three precipitation datasets in streamflow simulation.

Rainfall dataset	Calibration: 2012–2015						Validation: 2016–2019					
	NSE	PBIAS	RSR	R^2	P-factor	R-factor	NSE	PBIAS	RSR	R^2	P-factor	R-factor
Gauge	0.84	16.70	0.39	0.88	0.65	0.33	0.84	20.00	0.40	0.89	0.60	0.22
R/A	0.88	-11.20	0.35	0.88	0.71	0.35	0.91	-2.60	0.30	0.92	0.69	0.23
GsMAP_G	0.54	35.8	0.68	0.59	0.52	0.29	0.54	29.30	0.68	0.61	0.57	0.22

underestimated them.

Fig. 6 further examines the monthly variation of PBIAS and RMSE that compared daily precipitation inputs from the R/A and GsMAP_G products with those derived from the Gauge dataset. The R/A product introduced daily rain rates over the Terauchi catchment higher than the Gauge dataset regardless of the season, as shown by the negative mean PBIAS. In the case of the GsMAP_G dataset, daily rainfall averaged over the study area varied between overestimated and underestimated, with a significant underestimation during July and August (about 20%). The GsMAP_G dataset resulted in larger daily precipitation errors than the R/A product, regardless of the season. These errors are significant during the rainy and Typhoon seasons (May–October). In July, when many extreme rainfalls occurred over the study area, the mean daily precipitation RMSE was about 19 mm/h for the GsMAP_G, while it was around 9 mm/d for the R/A scenario. According to the differences in precipitation inputs, we expect disparate simulated hydrographs compared to streamflow observations.

4.2. Performance of the SWAT model using different precipitation datasets

Fig. 7 compares the observed and simulated daily streamflow for the three scenarios during calibration and validation periods. Overall, all simulations captured the seasonal patterns of daily streamflow. The hydrographs showed a satisfactory agreement between daily observed and simulated streamflow. All the simulations underestimated flow peaks greater than 60 m^3/s, which generally present low occurrence probability. The tendency of the three precipitation datasets to underestimate these flow peaks was as the following: GsMAP_G greater than Gauge, greater than R/A. The zoom-in plots of the hydrographs on July 2012, July 2017, July 2018, and August 2019 clearly show this underestimation and are presented in Figure B1 (Appendix B).

Table 3 summarizes the values of statistical indicators used for evaluating the performances of the three simulation scenarios. The Gauge and R/A-based simulations outperformed the GsMAP_G in simulating daily streamflow at the outlet of the Terauchi catchment during the calibration and validation periods. The NSE values were between 0.84 and 0.91 for the Gauge and R/A models, while the NSE value was 0.54 for the GsMAP_G scenario. The Gauge and GsMAP_G scenarios underestimated daily streamflow by 16.70–20.00% and 29.30–35.80%, respectively. Conversely, the R/A dataset resulted in an overestimation of 2.60–11.20%. According to the recommendations of Moriasi et al., (2007, 2015), the R/A scenario achieved “very good” performances in simulating streamflow trends (R^2 and NSE) and residual variations (RSR) and “satisfactory ” performance in simulating average magnitudes (PBIAS). This latter

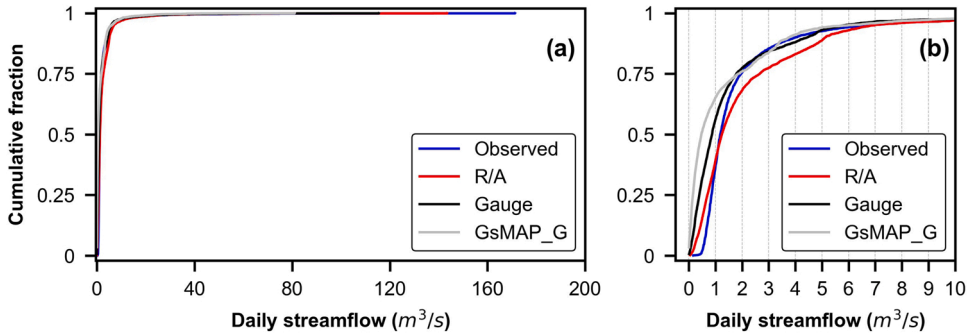

Fig. 8. Empirical cumulative distributions of daily simulated and observed streamflow.

Table 4
Statistical indicators values used for the evaluation of the SWAT models depending on streamflow exceedance probability.

Rainfall dataset	Extremely high streamflow		High streamflow		Average streamflow		Low streamflow	
	RMSE (m^3/s)	PBIAS (%)	RMSE (m^3/s)	PBIAS (%)	RMSE (m^3/s)	PBIAS (%)	RMSE (m^3/s)	PBIAS (%)
Gauge	24.10	28.47	3.07	8.85	0.83	14.05	0.47	35.24
R/A	16.55	17.45	3.33	-9.10	1.07	-20.25	0.50	-3.10
GsMAP_G	41.44	53.75	4.84	17.78	1.36	25.74	0.68	48.05

improved to "very good" during the validation period. The gauge-based model reached "very good" performances in terms of NSE and RSR and "good" performance in terms of R^2. However, it showed a "non-satisfactory" performance in simulating average magnitudes (PBIAS). On the other hand, the performance of the GsMAP_G model was "satisfactory" in simulating streamflow trends (R^2 and NSE) and residual variation and "non-satisfactory" in simulating average magnitudes.

Fig. 8 shows that the three precipitation datasets resulted in different streamflow CDF curves, especially for daily discharge less than 6 m^3/s (more than 90% of streamflow records) and daily flow greater than 60 m^3/s. For daily streamflow lower than 1 m^3/s, the cumulative fractions exhibited by the simulations were higher than the observations. From 1 m^3/s, the CDF of the R/A product deviated from the others to show lower cumulative fractions of simulated daily streamflow. These differences suggested that the performance of the evaluated precipitation datasets varied depending on streamflow intensity. Therefore, to better understand this variation, we categorized the daily observed streamflow into four ranges (Talchabhadel et al., 2021), based on the occurrence exceedance probability (OEP): 1) extremely high (OEP = 0–1%), high (OEP = 1–10%), average (OEP= 10–60%), and low (OEP= 60–100%). For each streamflow zone, the performance of each scenario was evaluated by computing the PBIAS and RMSE between simulated and observed discharge (Table 4).

The three models underestimated extremely high streamflow, with an advantage to the R/A simulation that represented the lowest biases (PBIAS = 17.45%) and errors (RMSE = 16.55 m^3/s). For the high and average streamflow ranges, the Gauge and GsMAP_G datasets underestimated daily streamflow (PBIAS = 8.85–25.74%), with an RMSE range of 0.83–4.84 m^3/s. Conversely, the R/A model overestimated daily streamflow by 9.10–20.25%, as shown in the PBIAS values, and introduced simulation RMSE of 1.07–3.33 m^3/s. For the low streamflow category, the Gauge and GsMAP_G scenarios significantly underestimated daily streamflow (PBIAS = 35.24% and 48.05%, respectively). On the other hand, the R/A dataset resulted in a PBIAS of − 3.10%, meaning an overestimation of daily streamflow.

4.3. Uncertainty in streamflow simulation

The uncertainty analysis was performed for the three simulations using the SUFI2 procedure. The values of P-Factor and R-Factor, computed for evaluating the prediction uncertainty, are shown in Table 3. The three tested datasets presented a narrow 95PPU envelope (R-Factor = 0.22–0.35) during the calibration and validation periods. Considering the P-factor that measures the fraction of observed streamflow within the 95PPU band, the R/A-based model exhibited the lowest prediction uncertainty with a P-factor of 0.71 for the calibration step and 0.69 for the validation step. The Gauge and GsMAP_G models did not reach an acceptable prediction uncertainty being their P-factor was less than 0.70.

The fitted value and range of uncertainty of each parameter used in the calibration process are shown in Fig. 9. Overall, the three precipitation datasets used in this study resulted in different fitted values and uncertainty ranges. CN2, the most sensitive parameter of the auto-calibrated parameters, was raised by more than 35% in all models to increase surface runoff. Similar results were shown for the soil bulk density (Soil_BD) parameter that controls surface runoff and baseflow. In all simulations, the value of Sol_BD was raised by more than 45% to increase the surface runoff and decrease base flow. This increase was accompanied by a significant reduction of the soil available water capacity (SOL_AWC) and a high overland Manning "n" coefficient (OV_N) that influences the timing and volume of flow peaks.

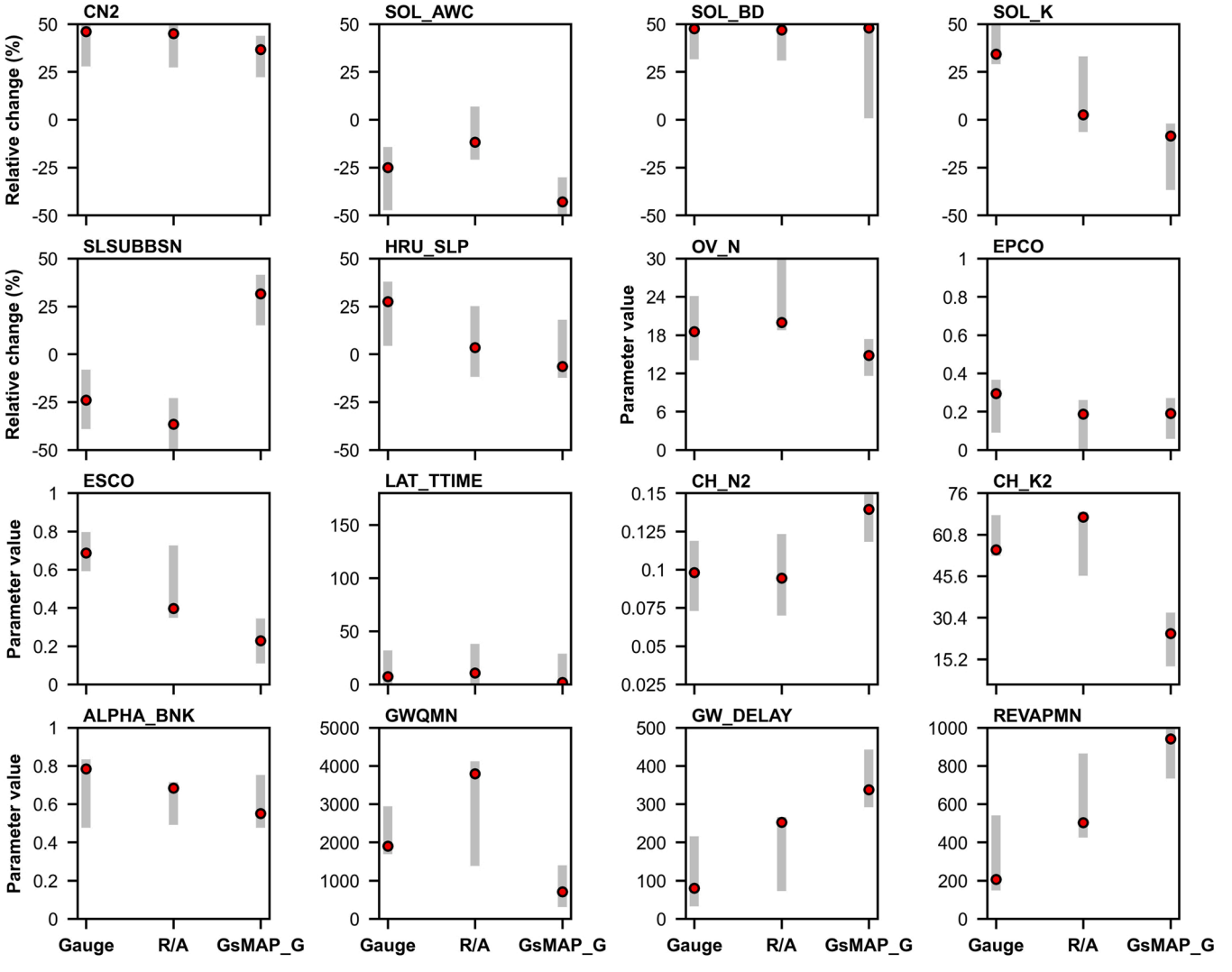

Fig. 9. Fitted parameters and their uncertainty ranges for the three simulation scenarios.

The Saturated hydraulic conductivity (SOL_K) indicates the ease of water movement through the soil profile. SLSUBBSN and HRU_SLP parameters are related to the topographic conditions in the study area. Together with the lateral flow travel time (LAT_TTIME), these three parameters impact lateral flow contribution to streamflow. During the calibration process, LAT_TTIME was low in all the simulations (1.78–10.70 days). In the Gauge scenario, the Sol_K and HRU_SLP were increased by 34.21% and 27.48%, respectively, allowing more lateral flow to the total streamflow. A similar trend was also observed for the R/A simulation, with a slight increase in SOL_K and HRU_SLP. Conversely, the calibration of the GsMAP_G model resulted in an opposite tendency for reducing the contribution of lateral flow to the total streamflow.

GWQMN, GW_DELAY, and REVAPMN parameters control the groundwater contribution to streamflow within the Terauchi catchment. ALPHA_BNK, the bank flow recession constant, determines the water contribution from bank storage to the main channel. While the three models shared relatively similar ALPHA_BNK, we noted significant variability in values and uncertainty ranges of the groundwater parameters. Compared to the Gauge and R/A models, GWQMN in the GsMAP_G scenario was lower (GWQMN = 707.01 mm), while GW_DELAY and REVAPMN were higher (GW_DELAY = 337.79 days; REVAPMN = 941.83 mm). The differences in fitted parameters resulted in different groundwater contributions to the catchment water balance.

ESCO and EPCO determine water allocation between evaporation and percolation. The ESCO parameter that governs soil evaporation within the SWAT model presented different fitted values in the three models. It was close to 0.70 in the Gauge model, indicating low soil evaporation. However, it was calibrated to 0.39 and 0.22 for the R/A and GsMAP_G models, resulting in increased evaporation and thus high potential evapotranspiration. On the other hand, all the three models shared relatively low EPCO allowing plant water uptake from the upper soil profile.

CH_N2 and CH_K2 correspond to Manning's "n" coefficient and hydraulic conductivity for the main channel. The calibrated values of the CH_N2 in the three models were in the range of 0.050–0.15, indicating that the main channel is mainly covered by heavy timber and brush. The CH_K2 in the Gauge and R/A scenarios reflected a moderately high loss rate. However, it suggested a moderate loss rate in the case of the GsMAP_G model.

4.4. Performances of the SWAT model using fixed parameters

The present analysis was carried out to avoid any possible bias caused by the auto-calibration of different input parameters in the SWAT model. We averaged the fitted parameters obtained for the three tested precipitation datasets. Subsequently, we run the SWAT model using the calibrated and averaged parameters for the total observation period (Table C1). Table C2 summarizes the performance indicators computed for the three simulations. Using fixed parameters, the performance of the Gauge and R/A models slightly decreased. Similar to the results obtained using calibrated parameters, the R/A model ranked the best in terms of streamflow simulation (NSE = 0.89), followed by the Gauge scenario (NSE = 0.83). On the other hand, the GsMAP_G scenario was sensitive to the change in model parameters, as its performance was lowered by 6% to become "non-satisfactory," with an NSE < 0.50 and RSR > 0.70.

5. Discussion

5.1. Evaluation of the R/A and GsMAP_G precipitation datasets

The statistical comparison between daily R/A precipitation estimates and gauge measurements revealed a strong correlation ($r > 90\%$) and accurate rainfall detection (CSI = 0.74). Literature showed that radar-based precipitation estimates are usually lower than gauge-based measurements (Schleiss et al., 2020; Seo et al., 2015). However, the R/A dataset used in the present study showed an opposite tendency. As shown in Fig. 2, the R/A datasets overestimated the precipitation by 15–38% in comparison with rain gauge measurements, causing higher average rainfall input in the SWAT model year-round (Fig. 6). Similarly, several previous comparisons demonstrated an overestimation of about 20% for the R/A product (Ishizaki and Matsuyama, 2018; Urita et al., 2011). This overestimation can be originated from the adjustment algorithm used for calibrating radars precipitation estimates by local rain gauge measurements. Indeed, the calibration process adopts the maximum value method, which selects the highest value when comparing grid point estimates and rain gauge measurements (Makihara, 2000).

Similar to the R/A dataset, GsMAP_G precipitation estimates were in good agreement with gauge measurements ($r > 80\%$) (Fig. 3). However, rainfall detection accuracy was significantly lower (CSI = 0.37), and daily estimates were generally underestimated, causing less water input in the SWAT model, especially in July and August (Figs. 5 and 6a). The low rainfall detection generally originated from sampling errors in the passive microwave images (Kubota et al., 2009). It is also related to the limitations of infrared and microwave sensors in capturing orographic, localized, and convective rainfall events (Hayashi et al., 2021; Nepal et al., 2021). This was reflected in the significant rainfall estimation errors (RMSE) by the GsMAP_G over the Terauchi catchment, which was observed during the rainy and Typhoon seasons (May–October) when heavy and orographic rainfalls are frequent (Fig. 6b). These estimation uncertainties implied the inefficiency of calibrating precipitation estimates based on only the 24 h accumulated rainfall amounts derived from the NOAA/CPC rain gauge-based product. They further suggested the need for updating the bias-adjustment algorithm (Mega et al., 2019) and the orographic rainfall correction scheme (Yamamoto and Shige, 2015) or the use of more local rain gauges (Deng et al., 2019) to improve the quality of the product and extreme rainfall detection.

5.2. Implication of the selection of precipitation datasets in streamflow simulation

The three precipitation datasets evaluated in the current study presented different measures, detection accuracy, and spatial

representation of the rainfall (R/A: approximately 1 km^2; Gauge: around 400 cm^2; GsMAP_G: about 120 km^2). These differences resulted in disparate rainfall inputs (e.g., dry days fractions and daily rainfall volume over the catchment) to the SWAT model and different streamflow simulation outputs. From the statistical indicators shown in Table 3, it was clear that the R/A dataset outperformed the other evaluated datasets in simulating daily streamflow at the Terauchi catchment. The low GsMAP_G model performance (NSE = 0.54) was faced with significantly higher performance in the case of the Gauge dataset (NSE = 0.84). This significant difference was also observed during the fixed-parameters model test (Table C2). Therefore, it is most likely due to the intrinsic underestimation of rainfall originating from the GsMAP_G product, knowing that the two datasets presented a similar spatial resolution. This finding is consistent with the study of Deng et al. (2019), who revealed the outperformance of the gauge-based model on the GsMAP_G dataset in a large basin (159 000 km^2) in China.

Extremely high (OEP < 1%) and low (OEP > 60%) flow events are generally difficult to reproduce in the SWAT model (Tan et al., 2020). These issues were reflected by the different occurrence fractions of daily streamflow less than 2 m^3/s in the simulations compared to the observations and the underestimation of flow peaks greater than 60 m^3/s (Figs. 7 and 8). One of the reasons is using only the NSE as an objective function during the auto-calibration process that reduced the mean differences and variances between simulated and observed streamflow but neglected the possible deviations in low flow periods (Krause et al., 2005). The R/A product partially overcame these issues as it improved the simulation of extremely high and low flow events (Table 4) compared to the Gauge and GsMAP_G datasets. This outperformance may not be only at the catchment scale but also at the sub-basin scale. The great performance of the R/A dataset was due to the high spatial resolution of the product (1 km) and the effective algorithm used for observing extreme rainfalls. Indeed, the high spatial resolution of the R/A product assists in capturing the detailed spatial features of precipitation, in particular the extreme convective events (Hirokawa et al., 2020; Kato, 2020; Sueki and Kajikawa, 2019; Tsuguti et al., 2019), responsible for the extremely high flow events in the study area. This led to overcoming the limitations of ground gauges in terms of spatial representation and measurement accuracy during extreme climatic conditions. The benefits of the R/A precipitation dataset in the SWAT model may, therefore, exceed the improvement of streamflow simulation to reach the study of hydro-climatic extremes (i.e., floods, droughts). Similar findings were also stated for a 2-km radar/rain gauge-adjusted product in Korea Cha and Lee (2021).

Although the study area presents static characteristics (i.e., land use, soil type, topography) during the simulation period, the evaluated precipitation datasets resulted in different model parameterization and discharge flux (Fig. 9). This is not surprising since the auto-calibration used in this study considered a wide range of uncertainty to search for the best set of parameters that optimize the fitting between observed and simulated streamflow. This variation leads to uncertain interpretations of the hydrological processes in the Terauchi catchment. The uncertainty can propagate towards other processes (e.g., sediment dynamics and contaminant transport) (Price et al., 2014). It would, therefore, affect the decision-making and may lead to different management and mitigation strategies. The situation would be more significant for the GsMAP_G dataset, which was the most sensitive to model parameterization. Therefore, the precipitation datasets in hydrological modeling should be selected with caution, considering their uncertainties and limitations.

6. Conclusions

Motivated by the potential of gauge-calibrated precipitation datasets in capturing the spatial pattern of rainfall with high accuracy and resolution, we investigated the usefulness of two datasets (radar-based: R/A and satellite-based: GsMAP_G) as input in the SWAT for daily streamflow simulation. The work focuses on the Terauchi watershed, a medium-size mountainous catchment in southwestern Japan. The research outcomes are in the following points:

- The R/A precipitation data were in good agreement with gauge observations. However, they are overestimated.
- The GsMAP_G underestimated the rainfall while found to be in correlation with gauge observations.
- The performance of the SWAT model forced with the three different precipitation datasets was as the following: R/A > Gauge > GsMAP_G.
- The R/A-based model was the most performant in simulating the streamflow with an NSE of > 88%.
- The R/A-based model improved the simulation of extremely high (OEP < 1%) and low (OEP > 60%) streamflow events.
- The three precipitation datasets resulted in different simulation outputs and model parameterization.

Overall, this work reveals the outperformance of the R/A product compared to the GsMAP_G and Gauge datasets in accurately representing the spatial variability of rainfall within the Terauchi catchment (51 km^2) and improving daily streamflow simulation using the SWAT model. However, the study outcomes are case-specific and expected to be true only in catchments with climate and scale similar to our study area. In a larger basin, the performance of the Gauge dataset can be improved due to a higher rain gauge density (Tan and Yang, 2020), which may lead to different conclusions regarding the “best” precipitation dataset in terms of streamflow modeling accuracy. Furthermore, the performances of the R/A and GsMAP_G products in other study sites with different topographic conditions and climate regimes (e.g., temperate and subarctic) may change due to the climate and attitude-dependent

propagation of precipitation uncertainty (Fallah et al., 2020; Nepal et al., 2021). Future research efforts should aim to validate the added value of the R/A product in improving streamflow simulation by focusing on other study areas with different climate and topographic conditions. Furthermore, they should assess the potential of other satellite-based datasets like the GPM-IMERG product, which outperformed the GsMAP_G in representing the spatial precipitation variability (Hsu et al., 2021). These future topics would provide interesting directions for improving the current algorithm used for producing the evaluated gauge-merged datasets and future constellation requirements (Kidd et al., 2021).

Funding

This work was supported by the project "Development of Technology for Impacts, Mitigation and Adaptation to Climate Change in The Sectors of Agriculture, Forestry and Fisheries" of the Agriculture, Forestry, and Fisheries Research Council (Japan).

Declaration of Competing Interest

The authors declare that they have no known competing financial interests or personal relationships that could have appeared to influence the work reported in this paper.

Acknowledgments

We thank the anonymous reviewers for their constructive comments. We further acknowledge the Japan Meteorological Agency, the Ministry of Land, Infrastructure, Transport and Tourism of Japan, and the Japan Aerospace Exploration Agency for freely providing the rain gauge rainfall data, streamflow data, and GsMAP_G precipitation dataset online.

Appendix A. Calculation methods of different statistics

The methods and equations used for computing the different statistics are described in this appendix.

$$r = \frac{\sum_{i=1}^{n}(x_i - \bar{x}) \quad (y_i - \bar{y})}{\sqrt{\sum_{i=1}^{n}(x_i - \bar{x})^2 \sum_{i=1}^{n}(y_i - \bar{y})^2}} \tag{A.1}$$

$$PBIAS = 100 \times \frac{\sum_{i=1}^{n}(x_i - y_i)}{\sum_{i=1}^{n} x_i} \tag{A.2}$$

$$RMSE = \sqrt{\frac{\sum_{i=1}^{n}(x_i - y_i)^2}{N}} \tag{A.3}$$

$$NSE = 1 - \frac{\sum_{i=1}^{n}(x_i - y_i)^2}{\sum_{i=1}^{n}(x_i - \bar{x})^2} \tag{A.4}$$

$$RSR = \frac{\sqrt{\sum_{i=1}^{n}(x_i - y_i)^2}}{\sqrt{\sum_{i=1}^{n}(x_i - \bar{x})^2}} \tag{A.5}$$

$$R^2 = \left(\frac{\sum_{i=1}^{n}(x_i - \bar{x}) \quad (y_i - \bar{y})}{\sqrt{\sum_{i=1}^{n}(x_i - \bar{x})^2 \sum_{i=1}^{n}(y_i - \bar{y})^2}} \right)^2 \tag{A.6}$$

x_i is the precipitation measured by rain gauge (mm) or observed streamflow (m^3/s) at day i. $\bar{x}$ is the mean of precipitation measured

Table A1
A 2 × 2 contingency table for evaluating the rainfall detection capabilities.

	Rain gauge observes rain	Rain-gauge observes no-rain
R/A or GsMAP_G estimates rain	a = hit	b = false alarm
R/A or GsMAP_G estimates no-rain	c = miss	d = correct negative

by rain gauge (mm) or mean observed streamflow (m^3/s). y_i is the precipitation estimated by gauge-adjusted datasets (mm) or simulated streamflow (m^3/s) at day *i*. $\bar{y}$ is the mean precipitation estimated by gauge-adjusted datasets (mm) or mean simulated streamflow (m^3/s). *N* is the number of observations.

The calculation of the categorical statistic metrics (POD, FAR, and CSI) was preceded by building a 2 × 2 contingency table that counts the hits and misses of the R/A and GsMAP_G datasets. A minimum of 1 mm of daily rainfall was used as a rain/no-rain threshold (Gao and Liu, 2013).

See Appendix Table A1.

Accordingly,

$$POD = \frac{a}{a + c} \tag{A.7}$$

$$FAR = \frac{b}{a + b} \tag{A.8}$$

$$CSI = \frac{a}{a + b + c} \tag{A.9}$$

Appendix B

See Fig. B1.

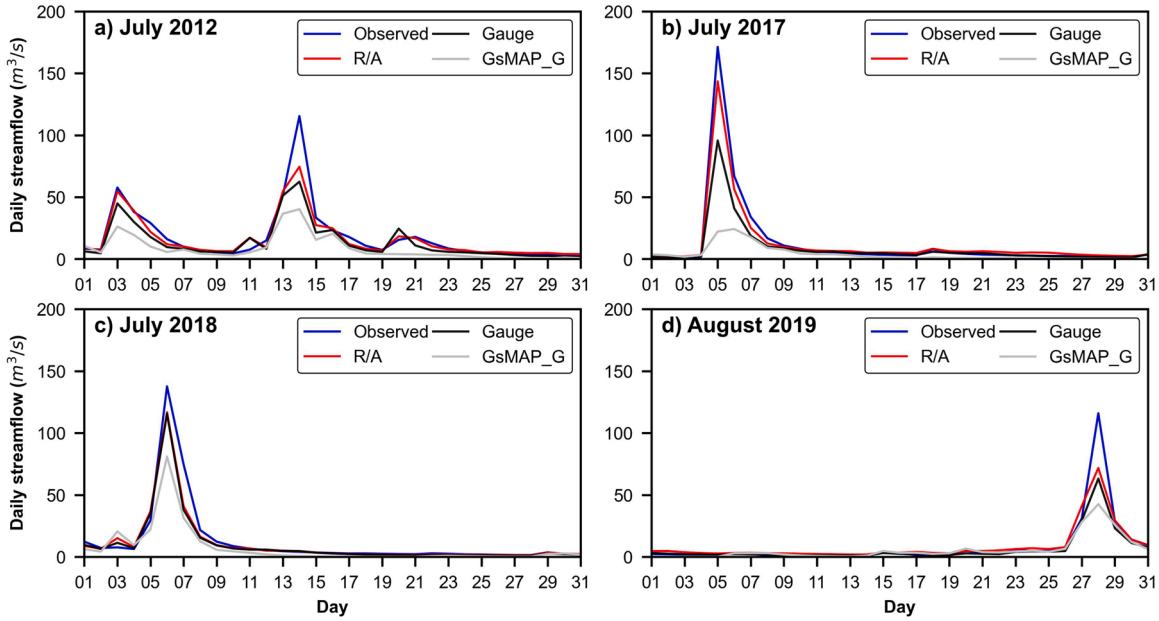

Fig. B1. Examples of underestimated flow peaks.

Appendix C. Model parameters and performance of the fixed-parameters simulations

See Tables C1 and C2.

Table C1
Averaged parameters values in the fixed parameters simulation tests.

Parameter	Averaged fitted value
r_CN2	+ 42.57%
r_SOL_AWC	+ 26.53%
r_SOL_BD	+ 47.48%
r_SOL_K	+ 9.38%
r_SLSUBBSN	- 9.67%
r_HRU_SLP	+ 8.18%
v_OV_N	17.77
v_EPCO	0.22
v_ESCO	0.43
v_LAT_TTIME	6.60
v_CH_N2	0.09
v_CH_K2	49.03
V_ALPHA_BNK	0.67
v_GWQMN	2251.66
v_GW_DELAY	223.44
v_REVAPMN	550.71

Table C2
Performances of the fixed-parameters and calibrated models in 2012–2019.

Rainfall dataset	Fixed parameters (2012–2019)			Calibrated parameters (2012–2019)		
	NSE	PBIAS	RSR	NSE	PBIAS	RSR
Gauge	0.83	20.00	0.41	0.84	18.40	0.40
R/A	0.89	-7.80	0.32	0.90	-6.70	0.32
GsMAP_G	0.48	32.80	0.72	0.54	32.40	0.68

Appendix D. Supporting information

Supplementary data associated with this article can be found in the online version at doi:10.1016/j.ejrh.2022.101134. These data include Google maps of the most important areas described in this article.

References

Abbaspour, K.C., 2014. SWAT Calibration and Uncertainty Programs—A User Manual, Eawag: Swiss Federal Institute of Aquatic Science and Technology.
Abbaspour, K.C., Johnson, C.A., van Genuchten, M.T., 2004. Estimating Uncertain Flow and Transport Parameters Using a Sequential Uncertainty Fitting Procedure. Vadose Zo. J. 3, 1340–1352. https://doi.org/10.2113/3.4.1340.
Abbaspour, K.C., Rouholahnejad, E., Vaghefi, S., Srinivasan, R., Yang, H., Kløve, B., 2015. A continental-scale hydrology and water quality model for Europe: Calibration and uncertainty of a high-resolution large-scale SWAT model. J. Hydrol. 524, 733–752. https://doi.org/10.1016/j.jhydrol.2015.03.027.
SCS, 1972. Section 4: hydrology. In: National Engineering Handbook. SCS.
Arnold, J., Allen, P., Muttiah, R., Bernhardt, G., 1995. Automated base flow separation and recession analysis techniques. Groundwater 33, 1010–1018 https://doi.org/doi.org/10.1111/j.1745-6584.1995.tb00046.x.
Arnold, J.G., Srinivasan, R., Muttiah, R.S., Williams, J.R., 1998. Large area hydrologic modeling and assesment Part I: model development. JAWRA J. Am. Water Resour. Assoc. 34, 73–89. https://doi.org/10.1111/j.1752-1688.1998.tb05961.x.
Arnold, J.G., Moriasi, D.N., Gassman, P.W., Abbaspour, K.C., White, M.J., Srinivasan, Santhi, R., Harmel, C., Griensven, R.D., VanLiew, a Van, Kannan, M.W., Jha, N., K, M., 2012. SWAT: Model use, calibration, and validation. Trans. ASABE 55, 1491–1508 https://doi.org/ISSN 2151-0032.
Cha, S.M., Lee, S.W., 2021. Advanced hydrological streamflow simulation in a watershed using adjusted radar-rainfall estimates as meteorological input data. J. Environ. Manag. 277, 111393 https://doi.org/10.1016/j.jenvman.2020.111393.
Chao, L., Zhang, K., Li, Z., Zhu, Y., Wang, J., Yu, Z., 2018. Geographically weighted regression based methods for merging satellite and gauge precipitation. J. Hydrol. 558, 275–289. https://doi.org/10.1016/j.jhydrol.2018.01.042.
Chen, M., Shi, W., Xie, P., Silva, V.B.S., Kousky, V.E., Higgins, R.W., Janowiak, J.E., 2008. Assessing objective techniques for gauge-based analyses of global daily precipitation. J. Geophys. Res. Atmos. 113, 1–13. https://doi.org/10.1029/2007JD009132.
Cho, J., Bosch, D., Lowrance, R., Strickland, T., Vellidis, G., 2009. Effect of spatial distribution of rainfall on temporal and spatial uncertainty of SWAT output. Trans. ASABE 52, 1545–1555. https://doi.org/10.13031/2013.29143.

Dembélé, M., Hrachowitz, M., Savenije, H.H.G., Mariéthoz, G., Schaefli, B., 2020. Improving the predictive skill of a distributed hydrological model by calibration on spatial patterns with multiple satellite data sets. Water Resour. Res. 56, 1–26. https://doi.org/10.1029/2019WR026085.
Deng, P., Zhang, M., Bing, J., Jia, J., Zhang, D., 2019. Evaluation of the GSMaP_Gauge products using rain gauge observations and SWAT model in the Upper Hanjiang River Basin. Atmos. Res. 219, 153–165. https://doi.org/10.1016/j.atmosres.2018.12.032.
Devia, G.K., Ganasri, B.P., Dwarakish, G.S., 2015. A review on hydrological models. Aquat. Procedia 4, 1001–1007. https://doi.org/10.1016/j.aqpro.2015.02.126.
Dinh, K.D., Anh, T.N., Nguyen, N.Y., Bui, D.D., Srinivasan, R., 2020. Evaluation of grid-based rainfall products and water balances over the Mekong river Basin. Remote Sens. 12 https://doi.org/10.3390/rs12111858.
Fallah, A., Sungmin, O., Orth, R., 2020. Climate-dependent propagation of precipitation uncertainty into the water cycle. Hydrol. Earth Syst. Sci. 24, 3725–3735. https://doi.org/10.5194/hess-24-3725-2020.
Gao, Y.C., Liu, M.F., 2013. Evaluation of high-resolution satellite precipitation products using rain gauge observations over the Tibetan Plateau. Hydrol. Earth Syst. Sci. 17, 837–849. https://doi.org/10.5194/hess-17-837-2013.
Gassman, P., Reyes, M.R., Green, C.H., Arnold, J.G., 2007. The soil and water assessment tool: historical development, applications, and future research directions. Trans. ASABE 50, 1211–1250. https://doi.org/10.13031/2013.23637.
Goudenhoofdt, E., Delobbe, L., 2009. Evaluation of radar-gauge merging methods for quantitative precipitation estimates. Hydrol. Earth Syst. Sci. 13, 195–203. https://doi.org/10.5194/hess-13-195-2009.
Hargreaves, G.L., Hargreaves, G.H., Riley, J.P., 1985. Agricultural benefits for senegal river basin. J. Irrig. Drain. Eng. 111, 113–124. https://doi.org/10.1061/(asce)0733-9437(1985)111:2(113).
Hayashi, Y., Tebakari, T., Hashimoto, A., 2021. A comparison between global satellite mapping of precipitation data and high-resolution radar data – a case study of localized torrential rainfall over japan. J. Disaster Res 16, 786–793. https://doi.org/10.20965/JDR.2021.P0786.
Hirokawa, Y., Kato, T., Tsuguti, H., Seino, N., 2020. Identification and classification of heavy rainfall areas and their characteristic features in Japan. J. Meteorol. Soc. Jpn. 98, 835–857. https://doi.org/10.2151/jmsj.2020-043.
Hsu, J., Huang, W.R., Liu, P.Y., 2021. Performance assessment of GPM-based near-real-time satellite products in depicting diurnal precipitation variation over Taiwan. J. Hydrol. Reg. Stud. 38, 100957 https://doi.org/10.1016/j.ejrh.2021.100957.
Ishizaki, H., Matsuyama, H., 2018. Distribution of the annual precipitation ratio of Radar/Raingauge-Analyzed Precipitation to AMeDAS across Japan. Sci. Online Lett. Atmos. 14, 192–196. https://doi.org/10.2151/SOLA.2018-034.
JAXA, 2014. Global Satellite Mapping of Precipitation (GSMaP) for GPM Algorithm Theoretical Basis Document (ATBD): Algorithm Theoretical Basis Document (ATBD): Algorithm Ver.6 17. https://doi.org/https://www.eorc.jaxa.jp/GPM/doc/algorithm/GSMaPforGPM_20140902_E.pdf.
Kato, T., 2020. Quasi-stationary band-shaped precipitation systems, named “senjo-kousuitai”, causing localized heavy rainfall in japan. J. Meteorol. Soc. Jpn. 98, 485–509. https://doi.org/10.2151/jmsj.2020-029.
Kawase, H., Imada, Y., Sasaki, H., Nakaegawa, T., Murata, A., Nosaka, M., Takayabu, I., 2019. Contribution of historical global warming to local-scale heavy precipitation in western japan estimated by large ensemble high-resolution simulations. J. Geophys. Res. Atmos. 124, 6093–6103. https://doi.org/10.1029/2018JD030155.
Kidd, C., Huffman, G., Maggioni, V., Chambon, P., Oki, R., 2021. The Global Satellite Precipitation Constellation: current status and future requirements. Bull. Am. Meteorol. Soc. 102, 1844–1861. https://doi.org/10.1175/BAMS-D-20-0299.1.
Krause, P., Boyle, D.P., Bäse, F., 2005. Comparison of different efficiency criteria for hydrological model assessment. Adv. Geosci. 5, 89–97. https://doi.org/10.5194/adgeo-5-89-2005.
Kubota, T., Ushio, T., Shige, S., Kida, S., Kachi, M., Okamoto, K., 2009. Verification of high-resolution satellite-based rainfall estimates around japan using a gauge-calibrated ground-radar dataset. J. Meteorol. Soc. Jpn. 203–222. https://doi.org/10.2151/jmsj.87a.203.
Li, D., Christakos, G., Ding, X., Wu, J., 2018. Adequacy of TRMM satellite rainfall data in driving the SWAT modeling of Tiaoxi catchment (Taihu lake basin, China). J. Hydrol. 556, 1139–1152. https://doi.org/10.1016/j.jhydrol.2017.01.006.
Li, H., Hong, Y., Xie, P., Gao, J., Niu, Z., Kirstetter, P., Yong, B., 2015. Variational merged of hourly gauge-satellite precipitation in China: Preliminary results. J. Geophys. Res. Atmos. 120, 9897–9915 https://doi.org/10.1002/ 2015JD023710.
Li, X., Long, D., Han, Z., Scanlon, B.R., Sun, Z., Han, P., Hou, A., 2019. Evapotranspiration estimation for tibetan plateau headwaters using conjoint terrestrial and atmospheric water balances and multisource remote sensing. Water Resour. Res. 55, 8608–8630. https://doi.org/10.1029/2019WR025196.
Lin, B., Chen, X., Yao, H., 2020. Threshold of sub-watersheds for SWAT to simulate hillslope sediment generation and its spatial variations. Ecol. Indic. 111, 106040 https://doi.org/10.1016/j.ecolind.2019.106040.
Makihara, Y., 2000. Algorithms for precipitation nowcasting focused on detailed analysis using radar and raingauge data. Tech. Reports Meteorol. Res. Institue.
McKee, J.L., Binns, A.D., 2016. A review of gauge–radar merging methods for quantitative precipitation estimation in hydrology. Can. Water Resour. J. 41, 186–203. https://doi.org/10.1080/07011784.2015.1064786.
Mega, T., Ushio, T., Matsuda, T., Kubota, T., Kachi, M., Oki, R., 2019. Gauge-adjusted global satellite mapping of precipitation. IEEE Trans. Geosci. Remote Sens. 57, 1928–1935. https://doi.org/10.1109/TGRS.2018.2870199.
Moriasi, D.N., Gitau, M.W., Pai, N., Daggupati, P., 2015. Hydrologic and water quality models: performance measures and evaluation criteria. Trans. ASABE 58, 1763–1785. https://doi.org/10.13031/trans.58.10715.
Moriasi, D.N., Arnold, J.G., Van Liew, M.W., Bingner, R.L., Harmel, R.D., Veith, T.L., 2007. Model evaluation guidelines for systematic quantification of accuracy in watershed simulations. Trans. ASABE 50, 885–900. https://doi.org/10.13031/2013.23153.
Nagata, K., 2011. Quantitative precipitation estimation and quantitative precipitation forecasting by the japan meteorological agency. RSMC Tokyo–Typhoon Cent. Tech. Rev. 13, 37–50 (https://doi.org/Online at). ⟨http://www.jma.go.jp/jma/jma-eng/jma-center/rsmc-hp-pub-eg/techrev/text13-2.pdf⟩.
Nanko, K., Ugawa, S., Hashimoto, S., Imaya, A., Kobayashi, M., Sakai, H., Ishizuka, S., Miura, S., Tanaka, N., Takahashi, M., Kaneko, S., 2014. A pedotransfer function for estimating bulk density of forest soil in Japan affected by volcanic ash. Geoderma 213, 36–45. https://doi.org/10.1016/j.geoderma.2013.07.025.
Nash, J., Sutclifee, J., 1970. River flow forecasting through conceptural models, part I - a discussion of principles. J. Hydrol. 10, 282–290. https://doi.org/10.1016/0022-1694(70)90255-6.
Neitsch, S.L., Arnold, J., Kiniry, J.R., Williams, J.R., 2011. Soil and Water Assessment Tool Theoretical Documentation Version 2009, Texas Water Resources Institute.
Nepal, B., Shrestha, D., Sharma, S., Shrestha, M.S., Aryal, D., Shrestha, N., 2021. Assessment of GPM-Era satellite products' (IMERG and GSMaP) ability to detect precipitation extremes over mountainous country nepal. Atmosphere (Basel) 12. https://doi.org/10.3390/atmos12020254.
Obara, H., Takata, Y., Kohyama, K., Maejima, Y., Wakabayashi, S., Kanda, T., 2016. A new soil map of Japan based on comprehensive soil classification system of Japan first approximation. Bull. Natl. Inst. Agro-Environ. Sci. 37, 133–148 https://doi.org/doi/10.24514/00003026.
Ochoa-Rodriguez, S., Wang, L.P., Willems, P., Onof, C., 2019. A review of radar-rain gauge data merging methods and their potential for urban hydrological applications. Water Resour. Res. 55, 6356–6391. https://doi.org/10.1029/2018WR023332.
Ogden, F.L., 2021. Geohydrology: hydrological modeling. Encycl. Geol. 457–476. https://doi.org/10.1016/B978-0-08-102908-4.00115-6 (Second Ed.
Price, K., Purucker, S.T., Kraemer, S.R., Babendreier, J.E., Knightes, C.D., 2014. Comparison of radar and gauge precipitation data in watershed models across varying spatial and temporal scales. Hydrol. Process. 28, 3505–3520. https://doi.org/10.1002/hyp.9890.
Schleiss, M., Olsson, J., Berg, P., Niemi, T., Kokkonen, T., Thorndahl, S., Nielsen, R., 2020. The accuracy of weather radar in heavy rain: a comparative study 3157–3188.
Schroeer, K., Kirchengast, G., Sungmin, O., 2018. Strong dependence of extreme convective precipitation intensities on gauge network density. Geophys. Res. Lett. 45, 8253–8263. https://doi.org/10.1029/2018GL077994.
Seo, B.C., Dolan, B., Krajewski, W.F., Rutledge, S.A., Petersen, W., 2015. Comparison of single- and dual-polarization-based rainfall estimates using NEXRAD data for the NASA Iowa flood studies project. J. Hydrometeorol. 16, 1658–1675. https://doi.org/10.1175/JHM-D-14-0169.1.
Singh, V.P., 2018. Hydrologic modeling: progress and future directions. Geosci. Lett. 5. https://doi.org/10.1186/s40562-018-0113-z.

Strauch, M., Lima, J.E.F.W., Volk, M., Lorz, C., Makeschin, F., 2013. The impact of Best Management Practices on simulated streamflow and sediment load in a Central Brazilian catchment. J. Environ. Manag. 127, S24–S36. https://doi.org/10.1016/j.jenvman.2013.01.014.

Sueki, K., Kajikawa, Y., 2019. Different precipitation systems between hiroshima and keihanshin during extreme rainfall event in western Japan in july 2018. J. Meteorol. Soc. Jpn. 97, 1221–1232. https://doi.org/10.2151/jmsj.2019-063.

Sun, Q., Miao, C., Duan, Q., Ashouri, H., Sorooshian, S., Hsu, K.L., 2018. A review of global precipitation data sets: data sources, estimation, and intercomparisons. Rev. Geophys. 56, 79–107. https://doi.org/10.1002/2017RG000574.

Suzuki, H., Nakakita, E., Takahashi, H., 2017. Accuracy of radar-rain gauge analyzed precipitation: analysis in kanto, koshin-etsu, and tohoku regions. Proc. Jpn. Soc. Civ. Eng. B1 Hydraul. Eng. 73, 13–18.

Talchabhadel, R., Aryal, A., Kawaike, K., Yamanoi, K., Nakagawa, H., Bhatta, B., et al. (2021). Evaluation of precipitation elasticity using precipitation data from ground and satellite-based estimates and watershed modeling in Western Nepal. *Journal of Hydrology: Regional Studies*, *33*(November 2020), 100768. https://doi.org/10.1016/j.ejrh.2020.100768.

Tan, M.L., Yang, X., 2020. Effect of rainfall station density, distribution and missing values on SWAT outputs in tropical region. J. Hydrol. 584, 124660 https://doi.org/10.1016/j.jhydrol.2020.124660.

Tan, M.L., Gassman, P.W., Yang, X., Haywood, J., 2020. A review of SWAT applications, performance and future needs for simulation of hydro-climatic extremes. Adv. Water Resour. 143, 103662 https://doi.org/10.1016/j.advwatres.2020.103662.

Tan, M.L., Gassman, P.W., Liang, J., Haywood, J.M., 2021. A review of alternative climate products for SWAT modelling: sources, assessment and future directions. Sci. Total Environ. 795, 148915 https://doi.org/10.1016/j.scitotenv.2021.148915.

Tapiador, F.J., Navarro, A., Levizzani, V., García-Ortega, E., Huffman, G.J., Kidd, C., Kucera, P.A., Kummerow, C.D., Masunaga, H., Petersen, W.A., Roca, R., Sánchez, J.L., Tao, W.K., Turk, F.J., 2017. Global precipitation measurements for validating climate models. Atmos. Res. 197, 1–20. https://doi.org/10.1016/j.atmosres.2017.06.021.

Tashima, T., Kubota, T., Mega, T., Ushio, T., Oki, R., 2020. Precipitation extremes monitoring using the near-real-time GSMaP product. IEEE J. Sel. Top. Appl. Earth Obs. Remote Sens 13, 5640–5651. https://doi.org/10.1109/JSTARS.2020.3014881.

Tobin, K.J., Bennett, M.E., 2009. Using SWAT to model streamflow in two river basins with ground and satellite precipitation data. J. Am. Water Resour. Assoc. 45, 253–271. https://doi.org/10.1111/j.1752-1688.2008.00276.x.

Tsuguti, H., Seino, N., Kawase, H., Imada, Y., Nakaegawa, T., Takayabu, I., 2019. Meteorological overview and mesoscale characteristics of the Heavy Rain Event of July 2018 in Japan. Landslides 16, 363–371. https://doi.org/10.1007/s10346-018-1098-6.

Tuo, Y., Duan, Z., Disse, M., Chiogna, G., 2016. Evaluation of precipitation input for SWAT modeling in Alpine catchment: a case study in the Adige river basin (Italy). Sci. Total Environ. 573, 66–82. https://doi.org/10.1016/j.scitotenv.2016.08.034.

Urita, S., Saito, H., Matsuyama, H., 2011. Temporal and spatial discontinuity of radar/raingauge-analyzed precipitation that appeared in relation to the modification of its spatial resolution. Hydrol. Res. Lett. 5, 37–41. https://doi.org/10.3178/hrl.5.37.

Wilks, D.S., 2011. Statistical methods in the atmospheric sciences: an introduction. International Geophysics Series, Third ed. Elsevier,.

Wu, K., Johnston, C.A., 2007. Hydrologic response to climatic variability in a Great Lakes Watershed: a case study with the SWAT model. J. Hydrol. 337, 187–199. https://doi.org/10.1016/j.jhydrol.2007.01.030.

Yamamoto, M.K., Shige, S., 2015. Implementation of an orographic/nonorographic rainfall classification scheme in the GSMaP algorithm for microwave radiometers. Atmos. Res. 163, 36–47. https://doi.org/10.1016/j.atmosres.2014.07.024.

Yang, Z., Hsu, K., Sorooshian, S., Xu, X., Braithwaite, D., Zhang, Y., Verbist, K.M.J., 2017. Merging high-resolution satellite-based precipitation fields and point-scale rain gauge measurements-a case study in Chile. J. Geophys. Res. 122, 5267–5284. https://doi.org/10.1002/2016JD026177.

Zhang, G., Su, X., Ayantobo, O.O., Feng, K., Guo, J., 2020. Remote-sensing precipitation and temperature evaluation using soil and water assessment tool with multiobjective calibration in the Shiyang River Basin, Northwest China. J. Hydrol. 590, 125416 https://doi.org/10.1016/j.jhydrol.2020.125416.

Zhong, L., Zhang, Z., Chen, L., Yang, J., Zou, F., 2016. Application of the Doppler weather radar in real-time quality control of hourly gauge precipitation in eastern China. Atmos. Res. 172–173, 109–118. https://doi.org/10.1016/j.atmosres.2015.12.016.